Wave Load Mitigation by Perforation of Monopiles

Andersen, Jacob; Abrahamsen, Rune; Andersen, Thomas Lykke; Andersen, Morten Thøtt; Baun, Torben Ladegaard; Neubauer, Jesper Lykkegaard

Published in:
Journal of Marine Science and Engineering

DOI (link to publication from Publisher):
10.3390/jmse8050352

Publication date:
2020

Document Version
Publisher's PDF, also known as Version of record

Journal of
Marine Science and Engineering

MDPI

Article

Wave Load Mitigation by Perforation of Monopiles

Jacob Andersen [1,*], Rune Abrahamsen [1], Thomas Lykke Andersen [1], Morten Thøtt Andersen [1], Torben Ladegaard Baun [2] and Jesper Lykkegaard Neubauer [2]

[1] Division of Reliability, Dynamics and Marine Engineering, Aalborg University (AAU), Thomas Manns Vej 23, 9220 Aalborg Øst, Denmark
[2] Vestas Wind Systems A/S, Hedeager 42, 8200 Aarhus N, Denmark
* Correspondence: jacoba@build.aau.dk

Received: 10 April 2020; Accepted: 9 May 2020; Published: 16 May 2020

Abstract: The design of large diameter monopiles (8–10 m) at intermediate to deep waters is largely driven by the fatigue limit state and mainly due to wave loads. The scope of the present paper is to assess the mitigation of wave loads on a monopile by perforation of the shell. The perforation design consists of elliptical holes in the vicinity of the splash zone. Wave loads are estimated for both regular and irregular waves through physical model tests in a wave flume. The test matrix includes waves with Keulegan–Carpenter (*KC*) numbers in the range 0.25 to 10 and covers both fatigue and ultimate limit states. Load reductions in the order of 6%–20% are found for *KC* numbers above 1.5. Significantly higher load reductions are found for *KC* numbers less than 1.5 and thus the potential to reduce fatigue wave loads has been demonstrated.

Keywords: wave loads; monopiles; perforation; hydrodynamics; wave flume tests

1. Introduction

The capacity of offshore wind energy in Europe is increasing relatively more than the onshore [1]. The relative increase in the offshore capacity over recent years may come as a result of the maturing of the offshore wind industry, where continuous optimization and development of know-how cause expenditures to drop. Levelized Cost of Energy (LCoE) for offshore wind energy has dropped more than 50% since 2013 [2].

In the offshore wind energy sector, monopiles are by far the most common foundation type. By 2018, more than 80% of the grid-connected offshore wind turbines in Europe were installed with monopiles [3]. The extensive use of monopiles has been key in driving down offshore wind LCoE. Monopiles have the benefits of simple manufacturing procedures and relatively quick installations, traditionally for water depths less than 30 m [4]. However, to utilize offshore wind power in the proximity of areas with challenging bathymetry or simply to locate wind turbines further offshore due to e.g., less visual impact or larger wind resources, wind turbines often need to be installed at locations with intermediate waters, 30 to 50 m, or even deep waters more than 50 m [3,5].

For bottom-fixed foundations, higher water depths increase the structural demands significantly. In intermediate and deep waters, jacket substructures are traditionally installed to obtain larger lateral stiffness and footprint to withstand mudline moments [6]. Wave load contributions to the fatigue lifetime of a jacket substructure is small, and in general wave and current loads on jacket substructures are less compared to monopiles [7]. Relative to monopiles, jackets further have the advantage of low material usage and low scour [6,8]. Nevertheless, the installation and manufacturing of jackets are costly and laborious relative to conventional monopiles, and especially fatigue design of joints may be costly [6,9].

Monopiles with extra large diameters ranging up to 10 m, can be a less costly substitute to jacket substructures at intermediate or deep waters. Application of large diameter monopiles at these depths

instead of jackets will maintain a relatively easy installation and manufacturing process, whilst some of the excessive know-how on monopiles can continue to be utilized [2].

The design of large diameter monopiles at intermediate to deep waters will ultimately be dominated by fatigue wave loads [8]. Optimizing the design of the substructure is recognized by [2,9] to be one of the highest potential cost reductions on offshore wind energy. According to [10], the share from substructures and foundations on the LCoE for bottom-fixed, offshore energy is approximately 13.5%. This is based on a reference case with 30 m water depth, 30 km to onshore interconnection, and 30 km to port for operation and maintenance.

Problem Statement

Vestas Wind Systems A/S has proposed an alternative design for large diameter monopiles (henceforth monopiles). The design includes perforation of a monopile with a diameter of 10 m aimed at locations with water depths of around 35–40 m. The perforation of the alternative monopile is concentrated in the vicinity of the free surface, cf. Figure 1.

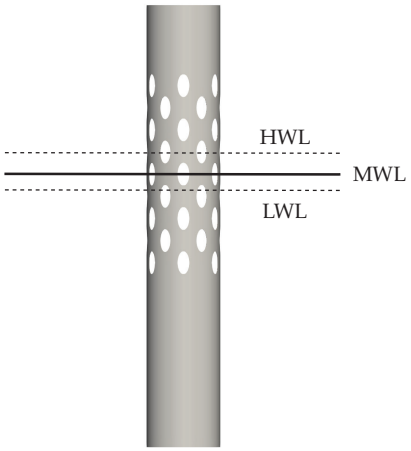

Figure 1. Conceptual illustration of the perforated monopile design with approximate mean water level (MWL) and water level variation (highest water level (HWL) to lowest water level (LWL)).

Perforation changes the flow pattern completely, thus the consequences with respect to loads are difficult to assess. However, as the perforation allows for a discharge through the monopile, it is expected that the perforation will decrease the downflow and associated horseshoe vortices, ultimately reducing the local scour. The run-up might also be decreased, due to the discharge of water through the monopile at wave impact. Cathodic protection of the interior of conventional monopiles has led to extreme water acidification and formation of hydrogen sulfide inside monopiles, which has caused special corrosive environments to develop. Perforation of monopiles to create a flow of ambient seawater through the interior of monopiles has been proved to mitigate the emerging of such corrosive environments [11]. Similar to artificial reefs, perforated monopiles have been found to cause fisheries and marine ecosystems to prosper [11].

Though being categorized as, and having the closest resemblance to a monopile, the perforated monopile has certain resemblances to a jacket substructure. The perforation may potentially enhance the monopile design by exploiting some of the advantages of a jacket substructure. In addition to the aforementioned indicated advantages, this includes mitigation of hydrodynamic loads, in particular fatigue wave loads.

The aim of the present paper is to examine the effect on mitigation of wave loads by perforation of monopiles. This is done by assessing the wave loads on a perforated and a conventional monopile through physical wave flume experiments.

2. Experimental Setup and Test Procedure

Hydraulic model tests were carried out in the wave flume of Department of Civil Engineering at Aalborg University, Denmark. The scale used in the model tests was 1:80. Unless otherwise specified, all values given in this paper are prototype values converted from model scale according to Froude model law.

Model tests were conducted for a monopile with a diameter of 10 m with 54 holes, see Figure 2. The 54 holes are placed in 12 equiangular spaced columns with 30 degrees interval, see Figure 2a,c. Every second column has 5 holes, and every second column has 4 holes. The model was oriented so that in the up-wave and down-wave directions there was always 5 holes. A conventional monopile was also tested as a reference. Henceforth, the models are referred to as 'the perforated monopile' and 'the reference monopile', respectively. It should be noted that neighboring columns of holes are overlapping with 0.1 m, see Figure 2a,b. The projected area of the perforated monopile oriented as seen in Figure 2a is approximately 89% of the projected area of the reference monopile. The models were tested sequentially and the generation file for each sea state was saved to use identical steering signals for wave generation with the two models.

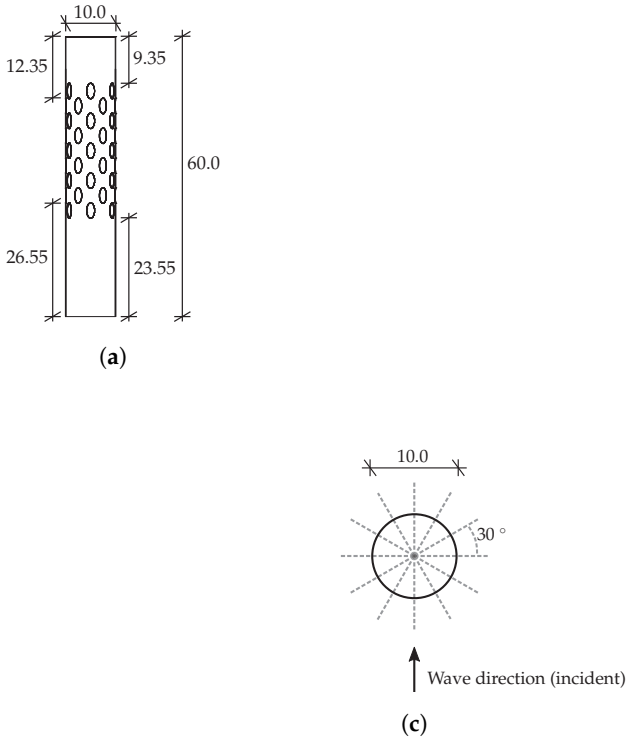

Figure 2. The perforated monopile. All measures are in m. (**a**) Perforated pile geometry as seen from the wavemaker. (**b**) Hole geometry. (**c**) Top view of the perforated pile. The dashed lines indicate the center lines of the elliptical holes.

The experimental setup in the wave flume is seen in Figures 3 and 4. Three perforated steel plates were installed close to the wavemaker, up-wave of the model position, in order to minimize transverse waves (cross-modes). The model was supported at the top by a load cell. The bottom of the flume was horizontal. The vertical distance between the models and the seabed was 3 mm (model scale). The models were placed in the middle between the flume side and an installed guide wall (a smooth steel plate). One wave gauge was installed in-line with the model, but behind the guide wall, see Figure 3a. The guide wall was installed in order to shield this wave gauge from diffracted waves from the model. A secondary wave gauge was installed approximately two meters in front of the model (up-wave). This wave gauge was installed to validate the measurements of the first wave gauge.

The thickness of the guide wall was 3.0 mm (model scale). Furthermore, in order to assess the wave height at the model position relative to the measured wave height behind the guide wall, the model was removed, and a wave gauge was installed at the model position. With this setup, selected sea states were repeated without the model in place.

The wave gauge behind the guide wall is seen to the right in Figure 4a. In the background of the photo the perforated plates for damping cross-modes can be seen in front of the piston wavemaker. It should be noted that the secondary wave gauge has not yet been installed in this photo. In Figure 4b, the perforated plates are visible in the foreground, and the secondary wave gauge up-wave of the perforated model has been installed.

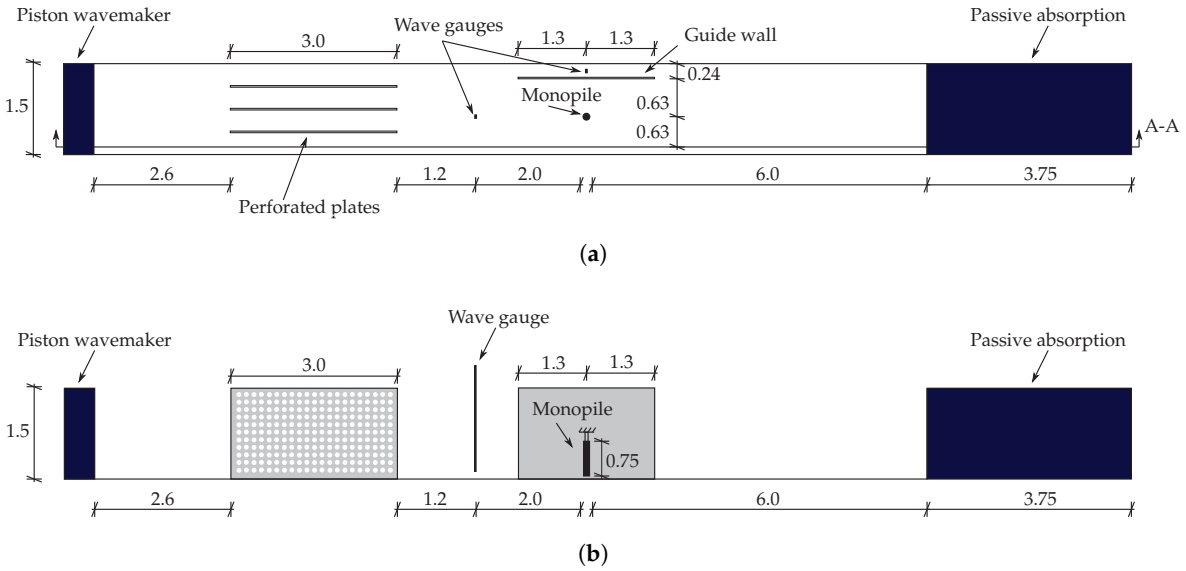

Figure 3. Setup of the wave flume used in the experiments. All measures are in m in model scale. (**a**) Wave flume seen from above. (**b**) Section A-A shown in (3a).

(**a**) (**b**)

Figure 4. Photos of the experimental setup in the wave flume. (**a**) Setup seen from the passive absorber. (**b**) Setup seen from the wavemaker.

The force transducer contained two electrical circuits each with four strain gauges set up in a full Wheatstone bridge to measure only bending in the wave propagation direction. The two circuits were placed with a spatial offset in the longitudinal direction of the transducer of 150 mm (model scale), which made it possible to calculate the horizontal force and its attack point. The output voltage from the strain gauge amplifiers (analogue signal) were measured and logged. The signal was filtered by an

analog low-pass filter with a cut-off frequency of 10 Hz (model scale). The logging of the signals from the force transducer and the wave gauges was done using the software package WaveLab 3.816 [12]. WaveLab was also used to calculate the eigenfrequencies and damping ratios by exciting the models by an impulsive load, see Table 1. Through WaveLab, the eigenfrequencies and damping ratios of the models were calculated whenever the water depth was changed or the model switched.

The output voltage signals from the force transducer were filtered from dynamic amplification by use of WaveLab. In regard to the dynamic amplification filtering, a low-pass cut-off frequency of 0.67 Hz (6 Hz in model scale) was applied for the reference monopile, and a cut-off frequency of 0.56 Hz (5 Hz in model scale) for the perforated monopile. Cut-off frequencies were chosen in order not to upscale noise. The reason for the difference in cut-off frequency is the difference in eigenfrequencies of the two models. The sample frequency was set to 11.2 Hz (100 Hz in model scale). The logging was initiated by a trigger signal from the wavemaker.

Table 1. Eigenfrequencies and damping ratios.

Water Depth [m]	Undamped Eigenfrequency [Hz]		Damping Ratio [-]	
	Perforated	Reference	Perforated	Reference
33	0.405	0.493	0.0224	0.0185
35	0.402	0.491	0.0202	0.0186
38	0.399	0.480	0.0207	0.0170

Tested Program

The wave parameters of the tests conducted in the physical wave flume are seen in Table 2. Sea states 11–16 were chosen in order to have three pairs of sea states with approximately the same Keulegan–Carpenter (KC) number in order to assess if this governs a potential load reduction. The KC number was calculated from

$$KC = \frac{u_{\max} T}{D},$$

where

T wave period,
D monopile diameter,
$u_{\max}$ maximum particle velocity at MWL.

$u_{\max}$ was calculated through stream function theory, i.e., in specific by application of the Fourier approximation method by [13]. The KC numbers were calculated based on the wave parameters in Table 2. The spectral significant wave height, H_{m0}, and the peak period, T_p, were applied in calculating KC numbers for the irregular sea states. Three different water depths, h, were investigated to see if typical variations of the water level, and thus location of the hole geometry relative to the water level, influenced any potential load reductions. The values in Table 2 are listed with mean values $+/-$ one standard deviation for the repeated sea states without the model in place. No repetitions were made for Sea states 3–5 and 9–10, and the values in Table 2 are from the wave gauge behind the guide wall with the reference monopile in place.

Regular waves were generated by approximate stream function (SF) wavemaker theory by [14] or second order wavemaker theory by [15] with modification by [16]. The minimum number of Fourier coefficients applied for the approximate stream function theory was $N = 10$.

The irregular sea states were generated from the inverse fast Fourier transform random phase method. The target spectrum was a JONSWAP spectrum with a peak enhancement factor of 3.3. Irregular waves were generated by second order wavemaker theory by [15] with modification by [16]. Active absorbtion was applied in order to minimize re-reflected waves [17]. The peak period, T_p,

and the significant wave height, H_{m0}, of Sea state 9 were so small in model scale that the high frequencies were truncated significantly.

Table 2. Tested sea states. H is the wave height, and T is the wave period.

Sea State	Type	Wavemaker Theory	h [m]	H or H_{m0} [m]	T or T_p [s]	KC [-]
1	Regular	Approx. SF.	38	19.2 ± 0.05	14.4	8.00
2	Regular	Approx. SF.	38	18.5 ± 0.20	16.4	9.02
3	Regular	Approx. SF.	33	16.3	14.4	7.39
4	Regular	Approx. SF.	33	16.1	16.4	8.54
5	Regular	2nd order	35	0.90	4.7	0.28
6	Regular	2nd order	35	3.8 ± 0.04	7.3	1.16
7	Regular	Approx. SF.	35	7.8 ± 0.03	11.8	2.94
8	Regular	Approx. SF.	35	10.8 ± 0.01	15.1	5.15
9	Irregular	2nd order	35	1.6	5.1	0.49
10	Irregular	2nd order	35	8.2	12.9	3.33
11	Regular	Approx. SF.	35	3.7 ± 0.02	14.9	1.70
12	Regular	Approx. SF.	35	4.6 ± 0.02	10.3	1.59
13	Regular	Approx. SF.	35	3.4 ± 0.02	20.4	2.12
14	Regular	Approx. SF.	35	4.1 ± 0.01	15.3	1.93
15	Regular	Approx. SF.	35	3.8 ± 0.01	20.1	2.35
16	Regular	Approx. SF.	35	4.5 ± 0.01	15.7	2.18

The wave force regimes of the sea states in Table 2 on a $D = 10$ m vertical cylinder are illustrated in Figure 5. The chart used in Figure 5 is given in [18], and is made under the assumption of linear theory. The sea state within the diffraction region is Sea state 5. The sea states within the inertia and drag region are Sea states 1–4.

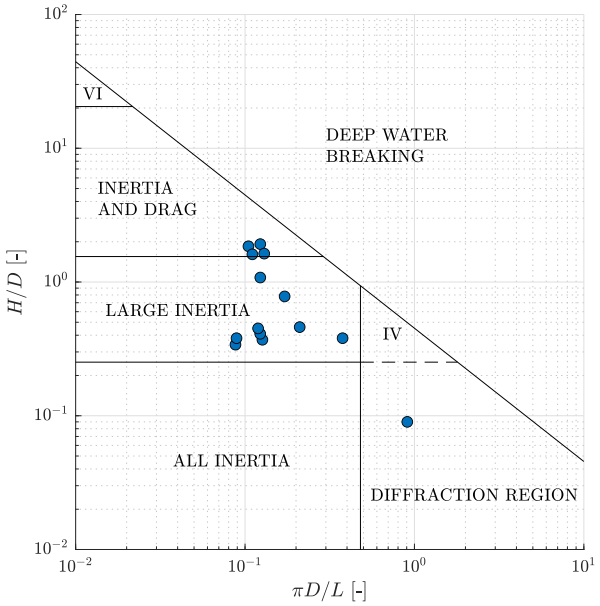

Figure 5. Graphical representation of the wave force regimes of tested sea states from Table 2.

3. Results

In the present section the results obtained from the physical wave flume tests are first presented for regular waves and subsequently for irregular waves. Finally, drag and inertia coefficients are calculated for the measured resulting force time series for regular waves using the Morison equation.

3.1. Regular Waves

The wavemaker was set with a ramp time of 10 s. The first fully developed wave was defined between two following zero-downcrossings, approximately 10 s after the first wave was visible in the wave gauge time series. The force history did not vary significantly after the selected first fully developed wave, and thus results are given for this wave. In Figure 6a, the wave heights measured behind the guide wall for the tests with the perforated monopile are shown relative to the tests with the reference monopile. In Figure 6b, the measured wave heights at model position without the model in place are shown relative to the wave heights measured behind the guide wall with the models in place (average of H_{perf} and H_{ref}) for the repeated sea states. All measured wave heights are given as absolute values in Appendix A.

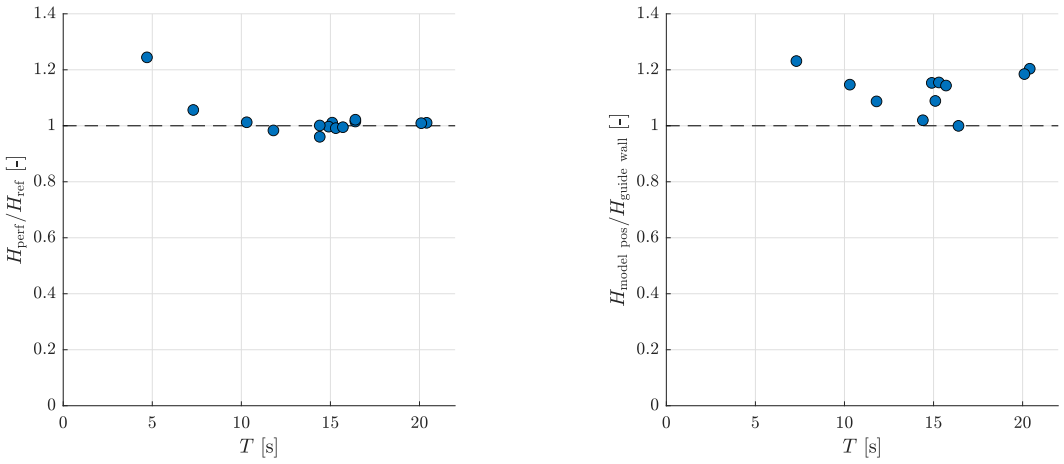

(**a**) (**b**)

Figure 6. Relative wave heights. (**a**) Wave heights for tests with the perforated monopile relative to wave heights for tests with the reference monopile. (**b**) Wave heights at model position without the model in place relative to the average wave heights behind the guide wall with the models in place.

Figure 6a shows that the measured wave heights for the reference monopile correspond well to the measured wave heights for the perforated monopile, allowing direct comparison of forces and moments acting on the two models. Sea state 5 ($T = 4.7$ s) differs as a rather high deviation between the measured wave heights is present (around 25%). In model scale, the wave height for this sea state was 1.4 cm, which makes deviations of the generated waves in the order of millimeters quite significant, relatively. Figure 6b shows that the measured wave heights behind the guide wall with the model in place are in average 10% lower than those in the model position without the model in place. This is ascribed to diffracted waves interfering with the incident waves. The scope of this paper is to assess the relative effect of perforation of monopiles. Hence, the deviation between measured waves heights behind the guide wall and at the model position in Figure 6b does not compromise the scope. However, in calculating the force coefficients the difference is important and thus values without the model in place are used for that purpose.

In Figure 7, the peak resulting force and mudline moment on the perforated monopile can be seen relative to the peak resulting force and mudline moment on the reference monopile, respectively. The asterisk, '*', denotes that the resulting forces and mudline moments have been normalized with respect to the respective measured wave heights by the wave gauge behind the guide wall, i.e., $F^* = F/H$ and $M^* = M/H$.

Uncertainties were quantified for the repeated sea states by sorting the resulting forces and mudline moments for the perforated monopile in descending order, and in ascending order for the reference monopile. The calculated ratio of each sea state were used to calculate the mean and standard deviation. Error bars indicating one standard deviation are included in Figure 7 for the sea states

where repetitions have been carried out. Five repetitions of Sea states 6 and 11–16 were performed. In order to increase the statistical certainty of the results for the higher waves, i.e., Sea states 1–4, five repetitions were carried out for Sea state 2. The water level for each load reduction is indicated by colors in Figure 7.

The reduction of peak loads, $\Gamma(KC)$, is described by a hyperbolic tangent function, see Equation (1), fitted to the normalized force reductions.

$$\Gamma(KC) = b \tanh(a\, KC). \tag{1}$$

Minimizing the squared error between Equation (1) and the normalized force reductions yields the coefficients; $a = 0.84$ and $b = 0.94$.

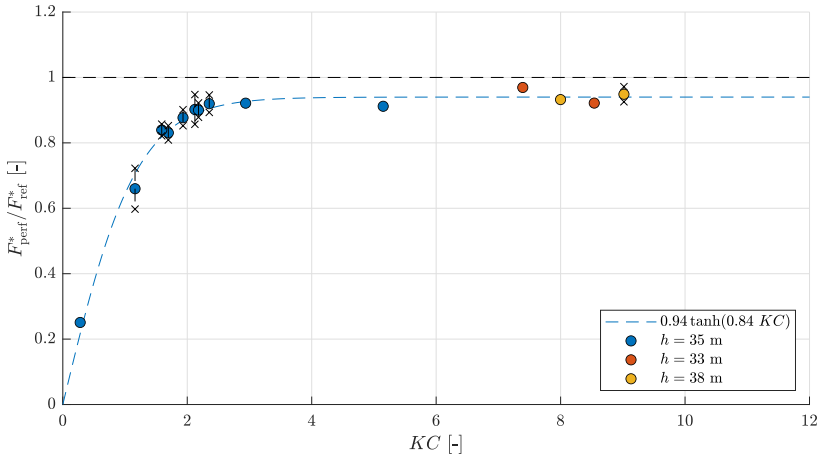

(**a**)

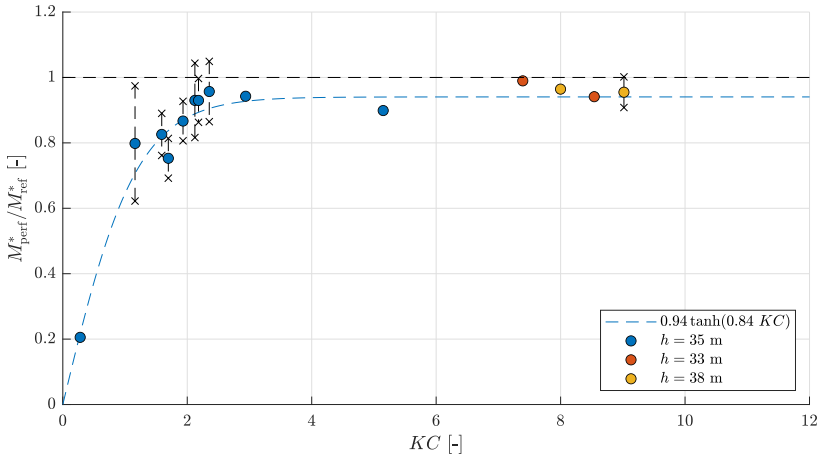

(**b**)

Figure 7. Load reduction for different Keulegan–Carpenter (KC) numbers and water levels. KC is calculated based on the measured wave parameters in Table 2. (**a**) Normalized resulting force on perforated monopile relative to reference monopile. (**b**) Normalized mudline moment on perforated monopile relative to reference monopile.

3.2. Irregular Waves

Two irregular sea states were tested; Sea states 9 and 10 in Table 2. In Figure 8, the mean, the mean of the highest third, the 98% fractile, and the maximum resulting force and mudline moment in the irregular model tests are given for the perforated monopile relative to the reference monopile. The characteristic values are found for the maxima of forces and moments, respectively. The KC

numbers are calculated based on the respective characteristic wave heights and periods. It is assumed that $T_{H_{2\%}} = T_{H_{1/3}}$. The values are calculated using WaveLab.

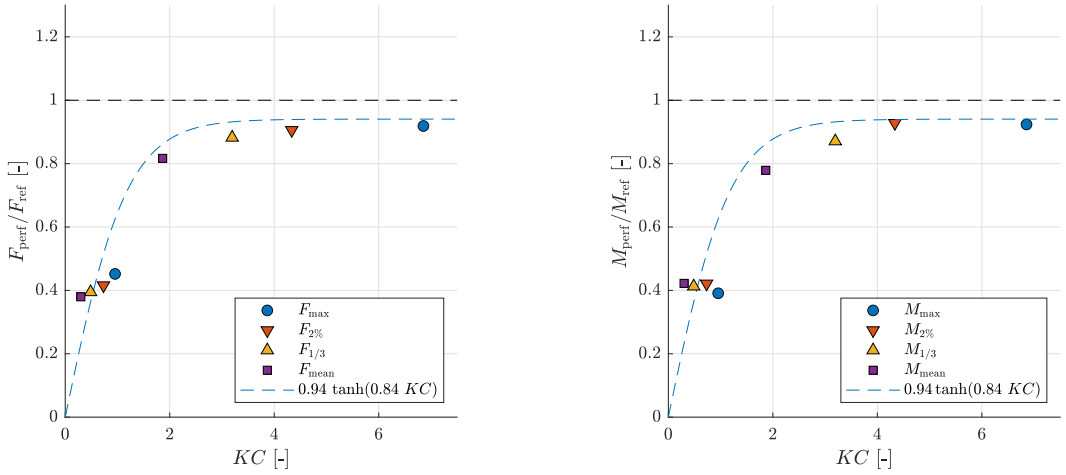

(**a**) (**b**)

Figure 8. Load reductions for the two irregular sea states. KC is calculated based on time domain analysis of the measured wave elevations. (**a**) Relative resulting forces. (**b**) Relative mudline moments.

3.3. Drag and Inertia by the Morison Equation

At the center of many engineering approaches of calculating wave loads is the Morison equation [19]. The Morison equation yields the distributed inline wave force to the flow direction per unit length, modeled as a sum of drag and inertia forces acting normal to the structure. The Morison equation applied to a vertical cylinder is seen in Equation (2) [20].

$$f(z,t) = \underbrace{\frac{\pi}{4}\rho C_M D^2 \frac{\mathrm{d}\left(u(x,z,t)\right)}{\mathrm{d}t}}_{\text{inertia}} + \underbrace{\frac{1}{2}\rho C_D D |u(x,z,t)| u(x,z,t)}_{\text{drag}}, \tag{2}$$

where

f	distributed Morison force (force per unit length of structure height),
ρ	density of water,
C_M	inertia coefficient,
D	structural diameter,
$u(x,z,t)$	horizontal particle velocity at the center line of the structure ($x = 0$),
C_D	drag coefficient.

The resulting Morison force (F) is found by integrating f from the sea bed to the surface. Drag and inertia coefficients strongly depend on the flow conditions and the geometry of the structure. Based on potential flow theory, the value of the inertia coefficients may be estimated. However, in most cases potential flow is not valid, and thus the coefficients are based on experimental work. Drag and inertia coefficients are given in [21] for prototype conditions (supercritical flow). For model scaled tests and more complex structures, such as the perforated monopile treated in the present paper, drag and inertia coefficients are determined experimentally. In the present paper a least square approach inspired by [22] is used, see Appendix B. Sea state 5 is in the diffraction regime (Figure 5) and is not considered. The wave kinematics are calculated from stream function theory based on the measured wave height, wave period, and water depth in each experiment. From Figure 6a, the effect from variations in wave heights within the same sea states are assessed to be negligible. The measured wave heights behind the guide wall with the model in place are underestimated due to diffraction from the model, see Figure 6b. An underestimation of wave height leads to underestimation of wave

kinematics. Thus to avoid an overestimation of the drag and inertia coefficients, the wave heights at model position are used as the basis for any calculation of force coefficients.

The measured surface elevations without the model in place are aligned with the those measured behind the guide wall with the model in place. Theoretical surface elevations are aligned with surface elevation zero-downcrossings at $\theta = 0$ and $\theta = 2\pi$. Figure 9a shows the measured surface elevation at the model location without the model in place and the theoretical surface elevation from stream function theory. The measured crest and trough are slightly underestimated. In Figure 9b,c, the force histories from the fitted drag and inertia coefficients are seen for all repetitions of Sea state 12. In order to capture the peak forces on the perforated monopile, force coefficients are scaled to give identical peak forces, see Figure 9c. Force coefficients are based on the entire structure height, even though the perforation only acts in the upper part of the water column.

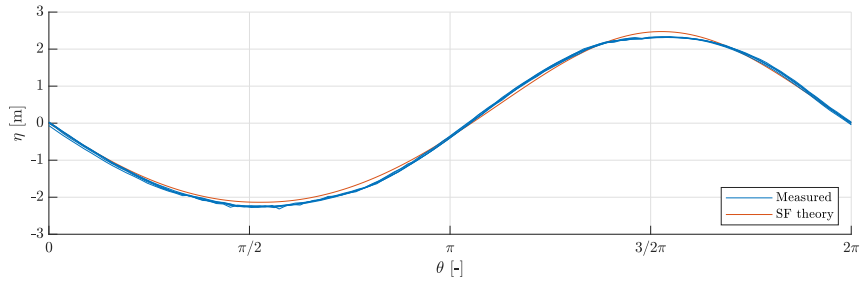

(**a**)

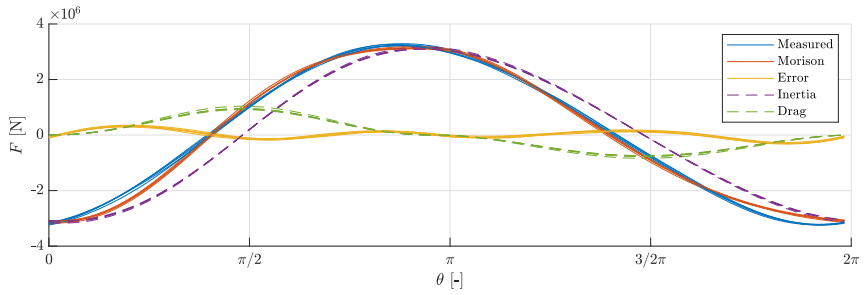

$C_M = 1.96 \pm 0.02$ and $C_D = 5.01 \pm 0.24$

(**b**)

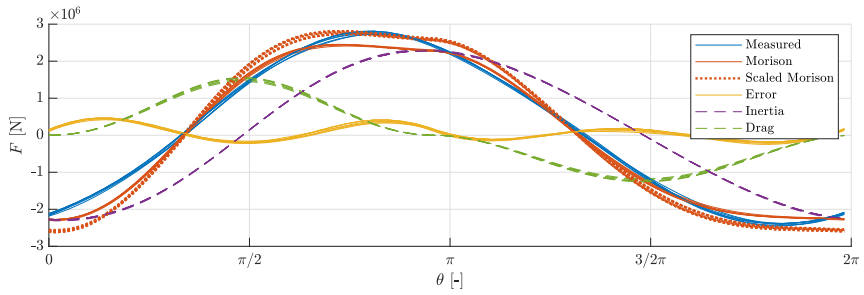

$C_M = 1.67 \pm 0.02$ and $C_D = 7.32 \pm 0.29$

(**c**)

Figure 9. Surface elevations and force histories for Sea state 12; $H = 4.6$ m, $T = 10.3$ s, $h = 35$ m, $KC = 1.59$. Wave heights are measured at the model location without the model in place. Force coefficients are given as the mean values +/− one standard deviation. (**a**) Surface elevation at model location. (**b**) Reference monopile. (**c**) Perforated monopile.

Figure 10a,b show the calculated force coefficients for both the perforated monopile (scaled to fit peak forces) and the reference (not scaled). Curves from experiments in [23] are included for relevant Reynolds numbers (Re). Re of the low KC sea states range from approximately 1.5×10^4 to 2.2×10^4. Re for the higher KC sea states are given in Figures 10a,b. Full correlation between the force coefficients

calculated for wave motions and the oscillating flow in a U-tube in [23] cannot be expected, due to the difference in velocity profiles, superharmonics, and free surface effects. It should be noted that the majority of the drag coefficients are calculated in the inertia dominated regime, and that these should not be ascribed high accuracy. Sea states 6 and 12 (lowest KC numbers) are excluded in Figure 10b due to brevity. All force coefficients are given in Appendix B.

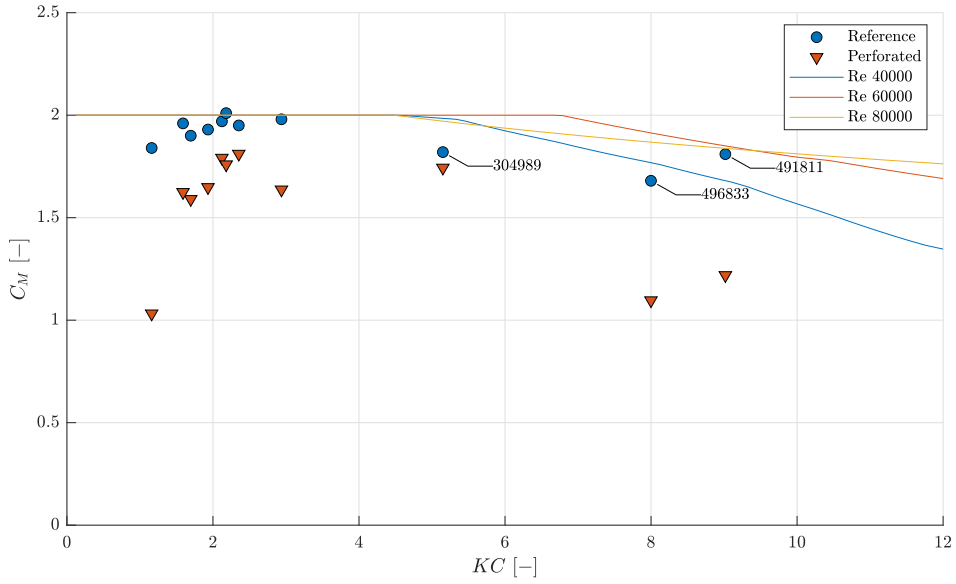

(a)

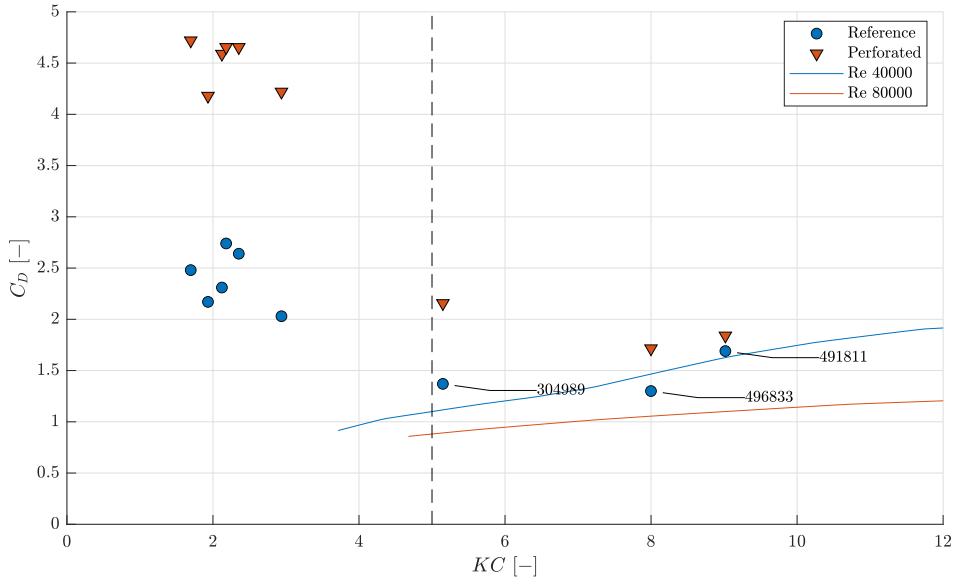

(b)

Figure 10. Mean value of force coefficients as function of KC based on mean wave heights measured without models in place. Lines are from [23]. (**a**) Inertia coefficients. (**b**) Drag coefficients. The vertical dashed line marks the upper limit of the inertia dominated region for a cylinder.

4. Discussion

The reduction of peak loads from the perforated design was found to be largest for Sea states 5 and 6, see Figure 7. The relative wave heights of Sea state 5 is associated with rather high uncertainties. However, as load reductions are based on normalized load peaks, and the load reduction of Sea state 5 is very substantial (calculated as 75%), this sea state does indicate the continuous increase of load

reductions as KC decreases at $KC < 1.5$. For Sea state 6, the reduction of the resulting force and mudline moment on the perforated monopile was approximately 30% and 20%, respectively. For KC numbers larger than 2, the load reduction stagnates at around 6% (as seen from $1 - b = 0.06$ in Equation (1)). From the tested typical variations of the water level, the load reductions seem invariant of the relative location of the hole geometry to the water level, see Figure 7. However, as the water level variations were only tested for high KC values (ULS cases), this trend still needs validation at low KC numbers. In general, the repeatability of the force reductions are high ($\pm$ 10%), while the moment reductions are associated with lower repeatability. From Figure 7, a rather significant load reduction is present for KC numbers lower than 2. Thus, the greatest load reductions from the perforation are in the inertia dominated regime. Correspondingly, the load reductions for the irregular waves are most significant for the lower KC numbers, see Figure 8. In Sea state 10 (the four highest KC numbers in Figure 8), the mean load reductions are largest. This observation is in accordance with the findings from the regular wave tests, as the mean load reduction is the load reduction in Figure 8 containing results from most low KC waves. The mean value does not differ to the same extent in Sea state 9, where all waves in the wave train are low KC waves.

The perforated monopile has a broader force peak due to an increase of the relative importance of drag, see Figure 9c. The maximal resulting force on the reference monopile is almost coinciding with the maximal inertia force as expected due to inertia domination at low KC numbers in accordance to [18], see Figure 9b. From Figure 9c, it follows that the Morison equation with the least square fitted force coefficients does not capture the force peaks on the perforated monopile correctly. Force coefficients for the perforated monopile are thus scaled up to fit the maximum absolute force peaks. The inertia contributions in all tested sea states are reduced for the perforated monopile compared to the reference. The extreme forces are decreased at zero-crossings where the magnitudes of the accelerations are largest. A broader force peak occurs, as the extreme forces shift towards the crest and troughs, i.e., an increased importance of drag.

Recommendations for Further Work

From the found wave load mitigation by the perforation of monopiles, it is recommended to further map the potential of perforated monopiles. For both regular and irregular sea states, the load reductions for $KC < 1.5$ were found to increase significantly, compared to $KC > 1.5$. The contribution from $KC < 1.5$ wave loads to the total fatigue lifetime should be estimated. This requires the stress concentration factors of the perforated monopile to be calculated, and furthermore the wave conditions of a given site to be known.

If $KC < 1.5$ wave loads are found to be significant for the total fatigue lifetime, it is recommended to conduct further model tests at $KC < 1.5$. In order to estimate the wave loads reductions at $KC < 1.5$ from wave flume experiments, the model to prototype scale must increase in order to mitigate uncertainties related to small wave heights and high wave frequencies. Thus, the tested irregular sea states at low KC numbers will not be as severely truncated as was seen for Sea state 9. Alternatively, numerical tests can be conducted.

Sea states with $KC > 10$ have not been investigated. Higher KC sea states increase the influence of drag. As the relative influence from drag is larger on the perforated monopile relative to a conventional monopile (see Table A2), the effect of the perforation for high KC sea states should be investigated as well.

In the present paper, the wave load reduction from the perforation of monopiles have only been estimated from model scale experiments. It is recommended to perform numerical experiments in prototype scale in order to estimate scale effects.

In order to map the commercial potential, a weight and cost comparison between a perforated and a conventional monopile should be carried out, and different production methods for the perforated monopile should be investigated, e.g., casting (in segments), segmented, and assembly. Furthermore, a stiffness analysis of the perforated monopile should be made, and influences on the performance

of the wind turbine generator assessed. It is also recommended to perform investigations on the mitigation of local scour and run-up by the perforation of monopiles in order to further map the potential. Larger holes in the perforated monopile design are expected to increase load reductions for higher KC numbers. An optimization study of the geometry, number, and spacing of holes is recommended with respect to both stress concentrations and load reductions.

5. Conclusions

In the present paper, the perforation of monopiles is found to mitigate wave loads. The load reductions are largest for sea states with low KC numbers, i.e., under fatigue wave conditions. Load reductions of approximately 10%–20% are found for both regular and irregular sea states with KC numbers between approximately 1.5 and 3. Significantly higher load reductions are found for $KC < 1.5$. For $KC > 5$, the load reductions are found to stagnate at around 6%. The reduction of forces and mudline moments are of the same order of magnitude. The repeatability is highest for the force reductions. Varying the water level relative to the hole geometry is not found to alter the load reductions.

The fit of drag and inertia coefficients based on the measured force histories yields a good prediction of the force histories on the reference monopile. The inertia coefficients are generally estimated with less uncertainty than the drag coefficients as most tested sea states are within the inertia dominated regime.

It should be stressed that the present paper only takes into account the mitigation of wave loads on a force and moment level and not on a stress level. The wave load mitigation is largest for fatigue sea states. The perforation introduces stress concentrations on the monopiles. Hence, the fatigue lifetime might not increase even though forces and moments on the perforated monopile decrease for fatigue sea states. The importance of the recommended further work is stressed by the authors.

Author Contributions: formal analysis, J.A. and R.A.; investigation, All; conceptualization, T.L.B. and J.L.N.; resources, T.L.A. and M.T.A.; data curation, J.A., R.A., T.L.A., and M.T.A.; writing—original draft preparation, J.A., R.A., and T.L.A.; writing—review and editing, J.A., R.A., T.L.A., and M.T.A.; supervision, T.L.A. and M.T.A; project administration, T.L.A., J.A., and R.A.; funding acquisition, T.L.A. All authors have read and agreed to the published version of the manuscript.

Funding: This research is supported by Vestas Wind Systems A/S.

Conflicts of Interest: The authors declare no conflict of interest.

Appendix A. Wave Heights

In Table A1, the wave heights measured from the wave gauge behind the guide wall are shown for all regular sea states in the test program. The wave heights measured from the repeated tests without the model in place are shown at model location and behind the guide wall.

Table A1. Measured wave heights for the regular sea state tests with and without the model in place.

Sea State	With Model		Without Model	
	H_{perf} [m]	H_{ref} [m]	$H_{\text{guide wall}}$ [m]	$H_{\text{model pos}}$ [m]
1	18.88	18.86	19.47 ± 0.03	19.24 ± 0.05
2	18.62 ± 0.19	18.34 ± 0.10	19.34 ± 0.42	18.47 ± 0.20
3	15.61	16.25		
4	16.49	16.14		
5	1.12	0.90		
6	3.18 ± 0.04	3.01 ± 0.10	3.55 ± 0.03	3.81 ± 0.04
7	7.10	7.22	7.76 ± 0.05	7.78 ± 0.03
8	9.99	9.88	10.66 ± 0.02	10.82 ± 0.01
11	3.18 ± 0.02	3.19 ± 0.02	3.46 ± 0.02	3.67 ± 0.02
12	4.04 ± 0.03	3.99 ± 0.02	4.37 ± 0.02	4.61 ± 0.02
13	2.85 ± 0.01	2.82 ± 0.01	3.15 ± 0.01	3.41 ± 0.02
14	3.53 ± 0.01	3.56 ± 0.02	3.91 ± 0.01	4.09 ± 0.01
15	3.26 ± 0.01	3.23 ± 0.01	3.61 ± 0.02	3.84 ± 0.01
16	3.93 ± 0.01	3.95 ± 0.02	4.33 ± 0.02	4.51 ± 0.01

Appendix B. Force Coefficients

The drag and inertia coefficients are calculated by a least square approach inspired by [22]. The squared error, ε, is integrated and minimized over one wave period, $\theta = \frac{2\pi}{T}t \in [0; 2\pi]$, see Equation (A1). Consequently, the calculated drag and inertia coefficients are time invariants.

$$\varepsilon = \int_0^{2\pi} \left(F_{\text{meas}} - F(C_D, C_M)\right)^2 \mathrm{d}\theta, \tag{A1}$$

where

F_{meas} measured resulting force time series,
$F(C_D, C_M)$ resulting Morison force time series calculated based on Equation (2).

The drag and inertia coefficients are calculated by minimizing ε in Equation (A1). Table A2 includes calculated drag and inertia coefficients based on the mean wave heights at model position, see Table A1. Only sea states tested without models in the wave flume are included.

Table A2. Fitted drag and inertia coefficients for regular sea states. Mean values with +/− one standard deviation are listed for the repeated sea states.

		Reference Monopile		**Perforated Monopile**		**Perforated Monopile Scaled Coefficients**	
Sea State	KC [−]	C_M [−]	C_D [−]	C_M [−]	C_D [−]	C_M [−]	C_D [−]
1	8.00	1.68	1.30	1.24	1.69	1.10	1.72
2	9.02	1.81 ± 0.02	1.69 ± 0.06	1.43 ± 0.04	2.16 ± 0.11	1.22 ± 0.04	1.84 ± 0.09
6	1.16	1.84 ± 0.02	15.75 ± 1.95	0.98 ± 0.01	14.18 ± 0.50	1.03 ± 0.02	14.96 ± 0.41
7	2.94	1.98	2.03	1.54	3.97	1.64	4.22
8	5.15	1.82	1.37	1.52	1.88	1.74	2.16
11	1.70	1.90 ± 0.03	2.48 ± 0.23	1.49 ± 0.02	4.42 ± 0.14	1.59 ± 0.03	4.72 ± 0.14
12	1.59	1.96 ± 0.02	5.01 ± 0.24	1.44 ± 0.01	7.85 ± 0.23	1.62 ± 0.01	8.88 ± 0.29
13	2.12	1.97 ± 0.02	2.31 ± 0.13	1.59 ± 0.01	4.08 ± 0.17	1.79 ± 0.02	4.59 ± 0.25
14	1.93	1.93 ± 0.01	2.17 ± 0.15	1.52 ± 0.01	3.90 ± 0.16	1.65 ± 0.03	4.18 ± 0.18
15	2.35	1.95 ± 0.02	2.64 ± 0.12	1.56 ± 0.02	4.01 ± 0.06	1.81 ± 0.03	4.65 ± 0.10
16	2.18	2.01 ± 0.02	2.74 ± 0.23	1.61 ± 0.02	4.27 ± 0.26	1.76 ± 0.01	4.66 ± 0.33

References

1. WindEurope. *Wind Energy in Europe in 2018, Trends and Statistics*; Walsh, C., Pineda, I., Eds.; WindEurope: Brussels, Belgium, 2019.
2. LEANWIND Consortium. *Driving Cost Reductions in Offshore Wind*; McAuliffe, F.D., Murphy, J., Lynch, K., Desmond, C., Norbeck, J.A., Nonås, L.M., Attari, Y., Doherty, P., Sørensen, J.D., Giebhardt, J., et al., Eds.; LEANWIND: Cork, Ireland, 2017.
3. WindEurope. *Offshore Wind in Europe, Key Trends and Statistics 2018*; Walsh, C., Ed.; WindEurope: Brussels, Belgium, 2019.
4. Bahaj, A.S.; Barnhart, C.J.; Bhattacharya, S.; Carbajales-Dale, M.; Cui, L.; Dai, K.; Dower, B.; Erdem, E.; Fried, L.; Gao, K.; et al. Civil Engineering Aspects of a Wind Farm. In *Wind Energy Engineering*, 1st ed.; Letcher, T.M., Ed.; Academic Press: Cambridge, MA, USA, 2017; ISBN: 978-0-12-809451-8.
5. IRENA (International Renewable Energy Agency). Floating Foundations: A Game Changer for Offshore Wind Power. *J. Phys. Conf. Ser.* **2016**, *753*, doi:10.1088/1742-6596/753/9/092003.
6. Schaumann, P.; Böker, C. Can Jackets and Tripods compete with Monopiles? In Proceedings of the Copenhagen Offshore Wind Conference, Copenhagen, Denmark, 26–28 October 2005.
7. Gong, W. Lattice Tower Design of Offshore Wind Turbine Support Structures. Master's Thesis, Norwegian University of Science and Technology (NTNU), Trondheim, Norway, June 2011.
8. Seidel, M. Substructures for offshore wind turbines—Current trends and developments. *Festschrift Peter Schaumann* **2014**, doi:10.2314/GBV:77999762X.

9. Damiani, R.; Dykes, K.; Scott, G. A comparison study of offshore wind support structures with monopiles and jackets for U.S. waters. *J. Phys. Conf. Ser.* **2016**, *753*, doi:10.1088/1742-6596/753/9/092003.
10. Stehly, T.; Beiter, P.; Heimiller, D.; Scott, G. *2017 Cost of Wind Energy Review*; National Renewable Energy Laboratory: Golden, CO, USA, 2018, doi:10.13140/RG.2.1.3111.6401.
11. Maher, M.M.; Swain, G.The Corrosion and Biofouling Characteristics of Sealed vs. Perforated Offshore Monopile Interiors, Experiment Design Comparing Corrosion and Environment Inside Steel Pipe. In Proceedings of the OCEANS 2018 MTS/IEEE Charleston, Charleston, SC, USA, 22–25 October 2018.
12. Frigaard, P.; Andersen, T.L. *Analysis of Waves: Technical Documentation for WaveLab 3*; Department of Civil Engineering, Aalborg University: Aalborg, Denmark, 2014, ISSN: 1901-7286.
13. Rienecker, M.M.; Fenton, J.D. A Fourier approximation for steady water waves. *J. Fluid Mech.* **1981**, *104*, doi:10.1017/S0022112081002851.
14. Zhang, H.; Schäffer, H.A. Approximate Stream Function wavemaker theory for highly non-linear waves in wave flumes. *Ocean Eng.* **2007**, *34*, doi:10.1016/j.oceaneng.2006.04.010.
15. Schäffer, H.A. Second-order wavemaker theory for irregular waves. *Ocean Eng.* **1996**, *23*, doi:10.1016/0029-8018(95)00013-B.
16. Eldrup, M.R.; Andersen, T.L. Applicability of Nonlinear Wavemaker Theory. *J. Mar. Sci. Eng.* **2019**, *7*, doi:10.3390/jmse7010014.
17. Andersen, T.L.; Clavero, M.; Frigaard, P.; Losada, M.; Puyol, J.I. A new active absorption system and its performance to linear and non-linear waves. *Coast. Eng.* **2016**, *114*, doi:10.1016/j.coastaleng.2016.04.010.
18. Chakrabarti, S.K. *Hydrodynamics on Offshore Structures*, 1st ed.; Springer: Berlin/Heidelberg, Germany, 1987; ISBN: 0-387-17319-6.
19. Morison, J. R.; O'Brien, M.; Johnson, J.; Schaaf, S. The Forces Exerted by Surface Waves on Piles. In *Petroleum Transactions*; AIME: New York, NY, USA, 1950; Volume 189.
20. Journée, J.M.J.; Massie, W.W. *Offshore Hydromechanics*, 1st ed.; Delft University of Technology: Delft, The Netherlands, 2001.
21. DNV GL AS. *DNVGL-ST-0437: Loads and Site Conditions for Wind Turbines*; DNV GL: Oslo, Norway, 2016.
22. Burcharth, H.F. Strøm- og Bølgekræfter på Stive Legemer (Danish), 2nd ed.; Aalborg Universitet: Aalborg, Denmark, 2002.
23. Sarpkaya, T. *Wave Forces on Offshore Structures*; Cambridge University Press: Cambridge, UK, 2014.